

# Microscale flow dynamics of red blood cells in microchannels: an experimental and numerical analysis

R. LIMA<sup>1,2</sup>, M. NAKAMURA<sup>3</sup>, T. OMORI<sup>1</sup>, T. ISHIKAWA<sup>1</sup>, S. WADA<sup>3</sup>, T. YAMAGUCHI<sup>1</sup>

1) Dept. Bioeng. & Robotics, Grad. Sch. Eng., Tohoku Univ., 6-6-01 Aoba, 980-8579 Sendai, Japan. 2) Dept. Mechanical Tech., ESTiG, Bragança Polyt., C. Sta. Apolonia, 5301-857 Bragança, Portugal. 3) Dept. Mechanical Science and Bioeng., Grad. Sch. Eng., Osaka Univ., Toyonaka, 560-8531 Osaka, Japan.

## 1 Introduction

Approximately, the half volume of the blood is composed of red blood cells (RBCs) which is believed to strongly influence its flow properties. Blood flow in microvessels depends strongly on the motion, deformation and interaction of RBCs. Several experimental studies on both individual and concentrated RBCs have already been performed in the past (Goldsmith 1971, Goldsmith and Marlow 1979, Chien et al. 1984, Goldsmith and Turitto 1986). However, all studies used conventional microscopes and also ghost cells to obtain visible trace RBCs through the microchannel. Recently, considerable progress in the development of confocal microscopy and consequent advantages of this microscope over the conventional microscopes have led to a new technique known as confocal micro-PIV (Tanaami et al. 2002, Park et al. 2004, Lima et al. 2006, 2007a). This technique combines the conventional PIV system with a spinning disk confocal microscope (SDCM). Due to its outstanding spatial filtering technique together with the multiple point light illumination system, this technique has the ability to obtain in-focus images with optical thickness less than 1  $\mu\text{m}$ .

In a numerical context, blood flow in large arteries is usually modeled as a continuum however this assumption is not valid in small vessels such

as arterioles and capillaries. In this way, we are developing an integrative multi-scale model to simulate the blood flow at mesoscopic level. This computational approach may provide important information on the rheology of blood in small vasculatures where non-Newtonian property of blood is not negligible.

The main purpose of this paper is to measure flow behavior of individual RBCs at different haematocrits (Hct) through a 75 $\mu$ m circular polydimethylsiloxane (PDMS) microchannel by means of confocal micro-PTV system. Moreover we introduce an integrative multi-scale model to simulate the blood flow behavior through microvessels in order to obtain more detailed insights about the blood rheological properties at cellular level.

## **2 Confocal micro-PTV measurements of RBCs**

### **2.1 Materials and methods**

#### ***2.1.1 Working fluids and microchannel***

Four working fluids were used in this study: dextran 40 (Dx40) containing about 3%(3Hct), 13% (13Hct), 23% (23Hct) and 37% (37Hct) of human RBCs. The blood was collected from a healthy adult volunteer, where ethylenediaminetetraacetic acid (EDTA) was added to prevent coagulation. The RBCs were separated from the bulk blood by centrifugation (1500 RPM for 5 minutes) and aspiration of the plasma and buffy coat and then washed twice with physiological saline (PS). The washed RBCs were labeled with a fluorescent cell tracker (CM-Dil, C-7000, Molecular Probes) and then diluted with Dx40 to make up the required RBCs concentration by volume (Lima 2007, Lima et al. 2008a). All blood samples were stored hermetical at 4°C until the experiment was performed at controlled temperature of about 37°C. All procedures in this experiment were carried out in compliance with the Ethics Committee on Clinical Investigation of Tohoku University.

By using a soft lithography technique it is possible to fabricate easily precise and reproducible rectangular microchannels at low cost. Rectangular PDMS microchannel with a low aspect ratio seems to be appropriate to perform confocal micro-PIV measurements of *in vitro* blood (Lima et al. 2008). However, this geometry may not reflect the actual physiology of the microcirculation. Hence, very recently we have successfully fabricated straight circular PDMS microchannels by using a wire casting technique (Lima 2007). The microchannel used in this study was a PDMS circular microchannel with a diameter of 75 $\mu$ m.

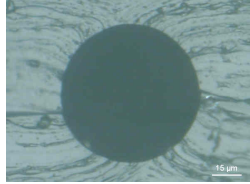


Figure 1. Cross section of the PDMS microchannel.

### 2.1.2 Confocal micro-PTV experimental set-up

The confocal micro-PIV system used in our experiment consists of an inverted microscope (IX71, Olympus, Japan) combined with a confocal scanning unit (CSU22, Yokogawa, Japan) and a diode-pumped solid state (DPSS) laser (Laser Quantum Ltd, UK) with an excitation wavelength of 532 nm. Moreover, a high-speed camera (Phantom v7.1, Vision Research, USA) was connected into the outlet port of the CSU22 (see Figure 2). The PDMS microchannel was placed on the stage of the inverted microscope where the flow rate of the working fluids was kept constant ( $Re \sim 0.004$ ) by means of a syringe pump (KD Scientific Inc., USA). A thermo plate controller was set to 37°C. All the confocal images were captured in the middle of the microchannels with a resolution of 640×480 pixels, at a rate of 100 frames/s with an exposure time of 9.4 ms. The recorded images were transferred to the computer and then evaluated in Image J (NIH) (Abramoff et al. 2004) by using a manual tracking MTrackJ (Meijering et al. 2006) plugin. As a result it was possible to track single RBCs through the middle plane of the PDMS microchannel.

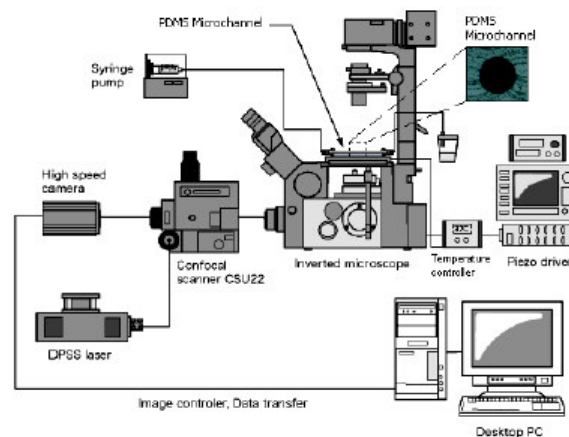


Figure 2. Experimental set-up.

### 2.1.3 RBC radial displacement and radial dispersion coefficient

The radial displacements ( $\Delta R$ ) of the tracked RBCs were determined by using the following equation:

$$\Delta R(t) = |R(t_0 + t) - R(t_0)| \quad (2.1)$$

where  $R(t)$  is the radial position at time  $t$ ,  $t_0$  is the initial time, and  $\Delta R(t)$  is the radial displacement at time interval  $t$ .

Besides the calculation of the radial displacement ( $\Delta R$ ), we have also analyzed the motions of RBCs by using a radial dispersion coefficient ( $D_{yy}$ ) (Goldsmith and Turitto 1986, Ishikawa and Pedley 2007), given by:

$$D_{yy}(t) = \frac{1}{N} \sum_{i=1}^N \frac{\langle (R_{i,y}(t) - R_{i,y}(0))^2 \rangle}{2t} \quad (2.2)$$

where  $R$ ,  $t$ ,  $N$  are the radial displacement, time interval and number of RBCs respectively.

## 2.2 Results and discussion

### 2.2.1 Blood flow visualization at several Hcts

Figure 3 shows images with both non-labeled RBCs (halogen illumination) and labeled RBCs (laser-emitted light) measured in centre plane of 75  $\mu\text{m}$  circular PDMS microchannel at several Hcts (from 3% to 37%) with  $Re$  from 0.004 to 0.005.

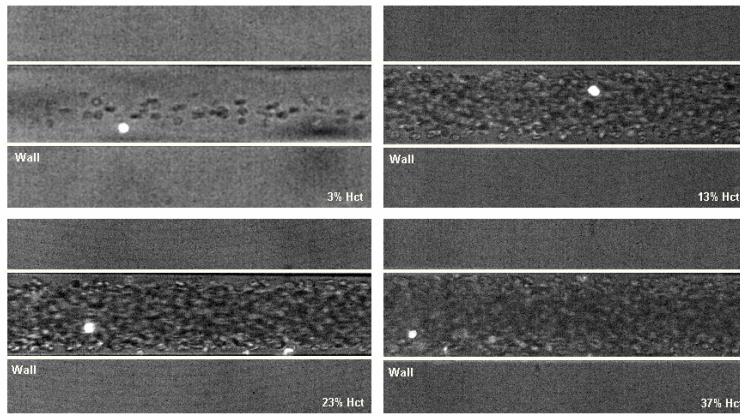


Figure 3. Both normal and labeled RBCs (bright spots) with 3% Hct, 13% Hct, 23% Hct, 37% Hct (20 $\times$ , 1.6 zoom).

From Figure 3 it is possible to observe that the Hct decreases with the microchannel diameter which corroborates with the well known Fahraeus effect (Chien et al. 1984). Moreover, it is also evident that the plasma layer tends to increase by decreasing the Hct (see Figures 4 and 5). This latter phenomenon is related to the Fahareues-Lindqvist effect (Fahareues and Lindqvist 1931). Although this phenomenon is still not completely understood (Caro 1979), the most acceptable explanation is related to the tendency of the RBCs to migrate toward the microtube axis enhanced by the RBCs deformation and interations (Schmid-Schonbein and Wells 1969, Goldsmith 1971). A further consequence is that the apparent blood viscosity is reduced so that the flow resistance through the capillary also decreases.

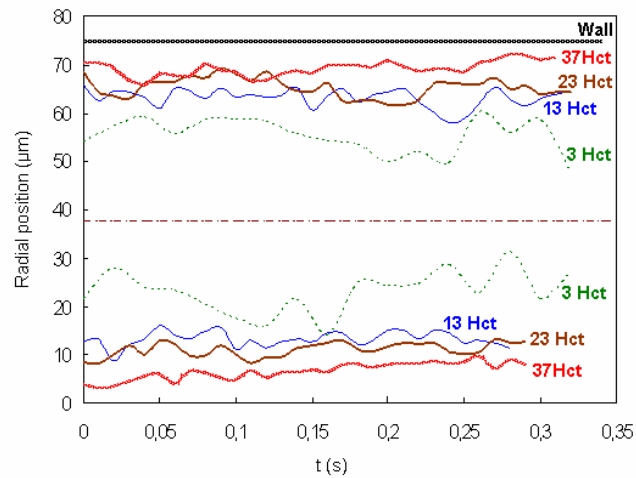


Figure 4. The effect of the Hct on the plasma layer.

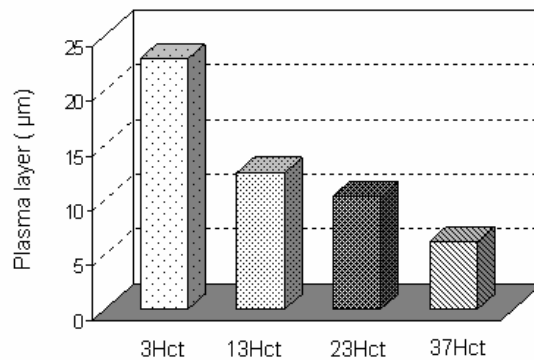


Figure 5. Average thickness of the plasma layer at several Hcts.

### 2.2.2 Radial displacement in a 75 $\mu\text{m}$ PDMS microchannel

Figure 6a shows the effect of the radial position on the motion of labeled RBCs flowing through a 75  $\mu\text{m}$  PDMS capillary, for a feed Hct of about 13%. In addition Figure 6b shows the radial displacement of a RBC flowing through microchannel with Hct of about 3%. The correspondent radial displacements ( $\Delta R$ ) are shown in Figure 7.

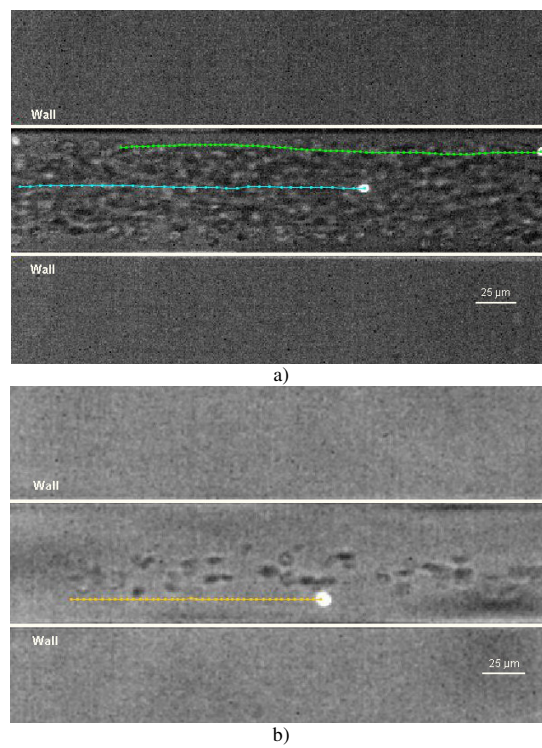


Figure 6. RBCs streamlines at several haematocrits: a) 13% Hct, b) 3% Hct.

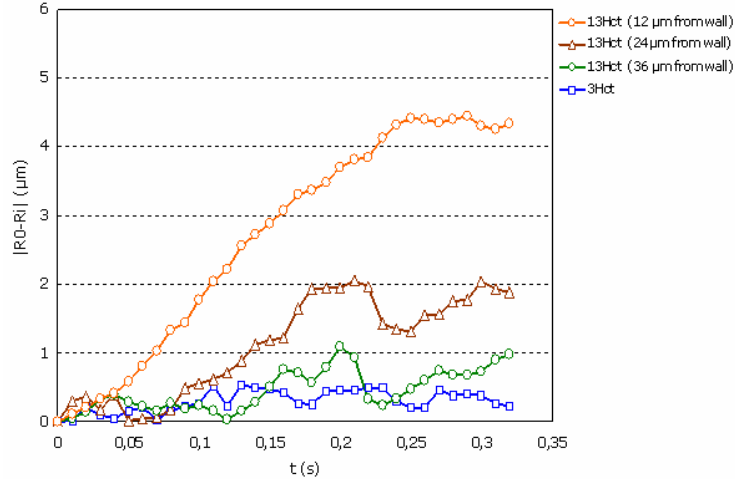


Figure 7. Radial displacement ( $\Delta R$ ) of labeled RBCs at several haematocrits (3% Hct and 13% Hct) and at different radial positions.

From Figure 7 it is clear that the RBCs radial displacement ( $\Delta R$ ) for 13% Hct is higher than a RBC flowing within an Hct of 3%. In addition it is also possible to observe that the radial displacement ( $\Delta R$ ) of the RBC flowing close to the plasma layer (12  $\mu\text{m}$  from the wall) is around 3 times higher than the RBC (36  $\mu\text{m}$  from the wall) traveling around the middle of the microchannel. These results suggest that RBCs flowing within the boundary region of RBC core appear to undergo the largest radial displacements. We believe that the random like transverse motions happening in this region are mainly due to multiple hydrodynamic interactions with neighboring RBCs which flow with lower velocity adjacent to the wall or tend to migrate away from the microtube wall towards the RBC region.

### 2.2.3 Radial dispersion in 75 $\mu\text{m}$ PDMS microchannel at several Hcts

By measuring the radial displacement of labeled RBCs flowing through the microchannel for a known time interval, it was possible to calculate the correspondent dispersion coefficient ( $D_{yy}$ ). Figure 8 shows the RBC averaged dispersion coefficient at the middle plane ( $D_{yy}$ ) for several Hcts (3% Hct, 13% Hct, 23% Hct and 37% Hct).

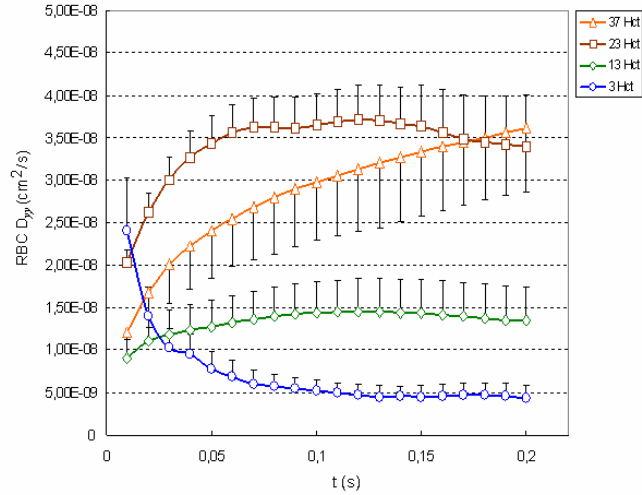


Figure 8. RBC averaged dispersion coefficient at the middle plane ( $D_{yy}$ ) for several Hcts: 3%Hct, 13%Hct, 23%Hct and 37% Hct.

Figure 8 shows that the radial dispersion coefficient ( $D_{yy}$ ) increases with the Hct. The RBC  $D_{yy}$  for Hcts from 23% to 37% have almost one order of magnitude greater than the  $D_{yy}$  with 3% Hct. These results clearly reflect the RBCs radial displacement obtained in Figure 7.

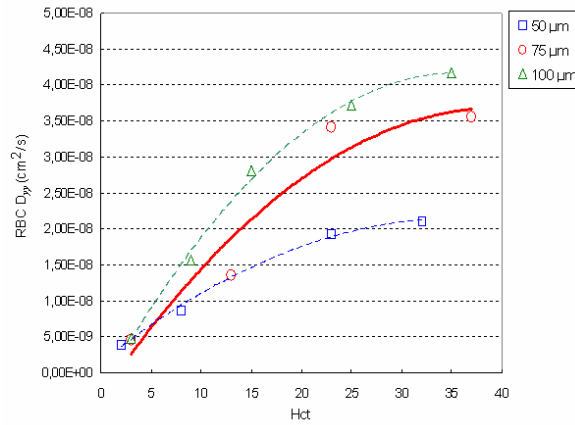


Figure 9. Effect of the Hct on the RBC  $D_{yy}$  at 75  $\mu\text{m}$  PDMS microchannel and 100 $\mu\text{m}$ , 50 $\mu\text{m}$  glass capillary (Lima et al. 2008).



Generally, our results demonstrate that the RBCs at dense concentrations exhibit higher erratic radial displacement when compared with diluted suspensions of RBCs. Although it is evident that the RBC radial dispersion rises with the increase of Hct at Hcts of about 24% it tends to level off (see Figure 9). Note that, these observations are consistent with several other measurements performed in glass microchannels (Goldsmith and Turitto 1986, Lima et al. 2008b).

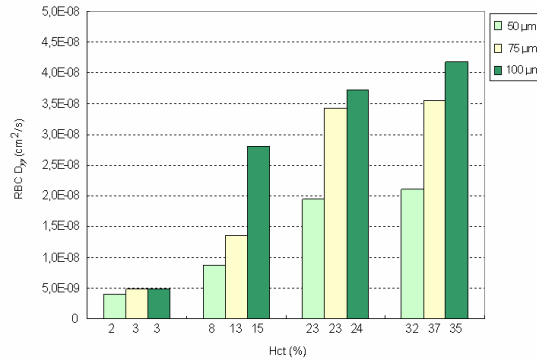


Figure 10. The effect of the microchannel diameter on the RBC  $D_{yy}$ .

The results from Figure 10 reinforce our previous measurements obtained from glass capillaries (Lima et al. 2008b). These data clearly demonstrate that RBC radial dispersion tend to decrease with the diameter. We believe that the main reason is due not only to Hct reduction with the diameter (Fahraeus effect) but also to the geometry constriction which limits the amplitude of the RBCs radial displacements.

### 3 Numerical flow model of multiple RBCs

A simulation method for multiple RBCs in a micro-vasculature was proposed for understanding the rheological properties of blood from a viewpoint of multiscale mechanics. In the following context, blood flow is modeled at two different scales. A micro-scale flow is modeled as a particulate flow of RBCs. On the other hand, flow at a macro-scale is modeled as a continuum expressed by the equations of continuity and Navier-Stokes. Then, a coupling method between those differently-scaled blood flow models is described. Finally, the simulation results are presented.

## 3.1 Materials and methods

### 3.1.1 Microscale blood flow model (RBC flow model)

An RBC model developed by Wada and Kobayashi (2003) was adopted. This model is capable of expressing a biconcave shape of the RBC at rest as well as its elastic deformation while in motion. As shown in Fig. 11, the model was constructed by surrounding the internal liquid of RBC with RBC membrane consisting of  $N$  nodal points linked by a spring element.

Owing to deformation, elastic energies are generated and stored in RBC. The stretching energy  $W_s$  and bending energy  $W_b$  are modeled as

$$W_s = \frac{1}{2} k_s \sum_{l=1}^N (L_l - L_{l0})^2 \quad (3.1)$$

$$W_b = \frac{1}{2} k_b \sum_{l=1}^{N_l} L_l \tan^2 \left( \frac{\theta_l}{2} \right) \quad (3.2)$$

where  $k_s$  and  $k_b$  are spring constants,  $N$ ,  $N_l$  are the number of nodes and lines,  $L_{l0}$ ,  $L_l$  are length of spring at the natural state and after deformation,  $\theta_l$  is the contacting angle between neighboring elements. To maintain the total area of RBC (actually it is volume in 3D), a penalty functions  $W_A$  was introduced. Mathematically, it was defined by

$$W_A = \frac{1}{2} k_A \left( \frac{A - A_0}{A_0} \right)^2 A_0, \quad (3.3)$$

where subscript 0 denotes the natural state,  $N_e$  is the number of bending springs,  $k_a$  is a coefficient for the area constraint.

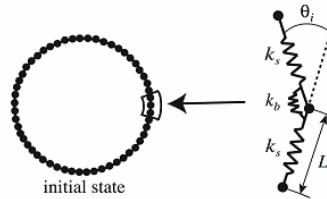


Figure 11. Red blood cell model. Nodal points on the membrane were connected by a mechanical spring. The neighboring springs were also linked by a bending spring.

An interactive force working between two RBCs which come closer are expressed by a potential function  $\Psi$  assigned at each nodal point on the

RBC membrane. The potential function  $\Psi$  for nodal point  $i$  is a summation of interactive forces from all neighboring nodal points as formulated by

$$\Psi = \sum_{i=1}^N \sum_{j=1}^N \Psi_{ij} \quad (3.4)$$

where  $\Psi_{ij}$  is the potential function on nodal point  $i$  from nodal point  $j$  on neighboring RBC. It is given by

$$\Psi_{ij} = \begin{cases} k_r \left( \frac{\pi z_{ij}}{2} - \tan \left( \frac{\pi z_{ij}}{2} \right) \right) & \text{for } -1 \leq z_{ij} \leq 0 \\ 0 & \text{for } 0 \leq z_{ij} \end{cases} \quad (3.5)$$

where  $z_{ij} = d_{ij}/\delta - 1$ ,  $d_{ij}$  is a distance between nodal points  $i$  and  $j$ , and  $\delta$  is equilibrium distance. According to this function, a repulsive force acts when they are come much closer. In the present simulation, the equilibrium distance  $\delta$  is set to  $L_0$  which is natural length of a spring.

An interactive force working between an RBC and a vessel wall is modeled in a way similar to the interactive force between two RBCs. The potential function  $Z$  for nodal point  $i$  is expressed by a summation of interactive forces from all neighboring nodal points as formulated by

$$Z = \sum_{i=1}^N Z_i \quad (3.6)$$

where  $Z_i$  is the potential function on nodal point  $i$  from nodal point  $j$  on neighboring RBC, which is given by

$$Z_i = \begin{cases} k_w \left( \frac{\pi z_i}{2} - \tan \left( \frac{\pi z_i}{2} \right) \right) & \text{for } -1 \leq z_i \leq 0 \\ 0 & \text{for } 0 \leq z_i \end{cases} \quad (3.7)$$

where  $z_i = D_i/\delta_w - 1$ ,  $D_i$  is the distance between nodal point  $i$  and the wall,  $k_w$  is a parameter to express the magnitude of a repulsive force, and  $\delta_w$  is an equilibrium distance. Here,  $\delta_w$  was set to the same as  $\delta$ .

Modeling of a fluid force  $\mathbf{f}_i$  working on an RBC is made separately for forces  $\mathbf{f}_{ni}$  and  $\mathbf{f}_{ti}$  which respectively work in normal and tangential directions to a line element  $i$  of an RBC membrane. On the basis of the conservation of momentum, the normal force,  $\mathbf{f}_{ni}$  working on a line element  $i$  of the RBC membrane is modeled as

$$\mathbf{f}_{ni} = \rho L_i \mathbf{v}_{ni}^2 \quad (3.8)$$

where  $\rho$  is a density of plasma, and  $\mathbf{v}_{ni}$  is a normal component of the velocity difference between an RBC and a plasma flow. The tangential force  $\mathbf{f}_t$  is modeled based on Newton's law of viscosity. If we assume that a flow

velocity at a distance  $\Delta$  from an RBC membrane is the same as a flow velocity at the RBC membrane, the tangential force  $\mathbf{f}_i$  that works on a line element  $i$  can be approximated as

$$\mathbf{f}_i = \mu_p L_i \mathbf{v}_i / \Delta \quad (3.9)$$

where  $\mu_p$  is a viscosity of plasma,  $\mathbf{v}_i$  is a tangential component of  $\mathbf{v}_i$ . The equivalent distance  $\Delta$  in Eq. (3.9) was estimated from Oseen flow theory where a two-dimensional cylinder with a radius of  $a$  falls down in a viscous fluid. The distance  $\Delta$  is therefore

$$\Delta = \left( 2.0 \left( \ln \frac{8.0}{\text{Re}} - \gamma \right) + 1.0 \right) \frac{a}{8.0} \quad (3.10)$$

where Re is the Reynolds number determined from a relative velocity of the cylinder to a fluid and a diameter of the cylinder and  $\gamma$  is Euler constant (= 0.57721). In the present study,  $a$  is set to be comparable to the size of an RBC. Note that the fluid force is assumed not to work when a distance between two RBCs is less than  $\delta$  for presuming the situation that they are in touch.

Given elastic energies and fluid forces, the motion of nodal point  $i$  placed on RBC membrane was determined from

$$m \ddot{\mathbf{r}}_i + \gamma (\dot{\mathbf{r}}_i - \dot{\mathbf{r}}_g) = \mathbf{F}_i + \mathbf{f}_i \quad (3.11)$$

where a dot means a time derivative,  $\mathbf{r}_i$  is the position vector of nodal point  $i$ ,  $m$  is mass of the nodal point, and  $\mathbf{f}_i$  is a fluid force (=  $\mathbf{f}_{ni} + \mathbf{f}_{mi}$ ). Based on the virtual work theory, an elastic force  $\mathbf{F}_i$  is given by

$$\mathbf{F}_i = \frac{\partial W}{\partial \mathbf{x}_i} \quad (3.12)$$

$$W = W_s + W_b + W_a + \Psi + Z. \quad (3.13)$$

### 3.1.2 Macroscale blood flow model (Continuum flow model)

A macroscale blood flow at a steady state is modeled as a continuum expressed by the Navier-Stokes and continuity equations;

$$u_j \frac{\partial u_i}{\partial x_j} = -\frac{\partial p}{\partial x_i} + \frac{1}{\text{Re}} \frac{\partial}{\partial x_j} \left( \frac{\partial u_i}{\partial x_j} + \frac{\partial u_j}{\partial x_i} \right) \quad (3.14)$$

$$\frac{\partial u_i}{\partial x_i} = 0 \quad (3.15)$$

where  $u_i$  is a flow velocity component and  $p$  is a pressure. In general, fluid viscosity is assumed to be spatially constant for the analysis of arterial

blood flow. However, it is not true in small arteries due to spatial variation of RBC concentration. We here introduce a Hematocrit function  $F(\text{Hct})$  to the viscous term of the Navier-Stokes equation in order to express a local viscosity dependent on a local hematocrit.

Blood flow is often represented by Casson model. Shiga et al. (1979) obtained an empirical formula of the relationship between Casson viscosity  $\eta_c$  and hematocrit Hct as

$$\ln\left(\frac{\eta_c}{\eta_p}\right) = k \cdot \text{Hct} \quad (3.16)$$

where  $\eta_p$  is a plasma viscosity and  $k$  is a constant. Based on this equation, we express the hematocrit function  $F$  as

$$F = \frac{\eta_c}{\eta_p} = \exp[k \cdot \text{Hct}], \quad (3.17)$$

whereby the Navier-Stokes equation is rewritten as

$$u_j \frac{\partial u_i}{\partial x_j} = -\frac{\partial p}{\partial x_i} + \frac{\exp[k \cdot \text{Hct}]}{\text{Re}} \frac{\partial}{\partial x_j} \left( \frac{\partial u_i}{\partial x_j} + \frac{\partial u_j}{\partial x_i} \right) \quad (3.18).$$

In the actual simulation of a macroscale flow, we solve Eqs. (3.15) and (3.18) by a finite element method.

### **3.1.3 Geometry model of a small vasculature**

The present study solved blood flowing between a two-dimensional parallel plate flow channel. The  $x$ -axis and  $y$ -axis were respectively set in axial and radial directions of the channel. For the microscale simulation, 108 RBCs were put in the channel with height of 96  $\mu\text{m}$  and length of 44  $\mu\text{m}$ . In this case, Hct is 0.31. A periodic boundary condition was assumed for both  $x$ -ends of the channel. For the macroscale flow analysis, the channel is extended to 480 mm. The flow region was divided into triangular finite elements. The total numbers of nodal points and elements were 2500 and 4752, respectively.

### **3.1.4 Simulation condition**

Table 1 encapsulates the parameter of the microscale flow. The Reynolds number was 0.6. Parameter  $k$  in Eq. (3.17) was set to 2.85 based on the viscosity of the whole blood of 4.55 mPa·s and that of the plasma of 1.33 mPa·s at Hct of 0.44, a shear rate of 230  $\text{s}^{-1}$ , and temperature of 37 °C.

Table 1 Parameters used for the simulation

Number of nodes, $N$	60
Mass, $m$	$1.0 \times 10^{-15}$ kg
Spring constant for stretching, $k_s$	$1.0 \times 10^{-17}$ J
Spring constant for bending, $k_b$	$1.0 \times 10^{-18}$ J
Spring constant for the area constraint, $k_a$	$1.0 \times 10^{-16}$ J
Viscosity of the red blood cell membrane, $\gamma$	$1.0 \times 10^{-10}$ kg/s

### 3.1.5 Simulation procedure

A flowchart of the simulation is shown in Fig. 12. Assuming with Poiseuille flow as an initial axial flow, the microscale flow is calculated. When the radial distribution of RBCs becomes stable, the calculation is stopped, and the Hct functions are obtained for flow segments defined by radially subdividing the flow channel by  $N$  to incorporate the influence of the local variation of an RBC distribution into the macroscale flow analysis. The macroscale flow simulation is performed until a fully-developed axial velocity profile is obtained. With this velocity profile, the simulation is back to the microscale simulation. This process is repeated until a change in the axial velocity profile after the microscale flow simulation is negligible. In the present simulation,  $N = 8$ .

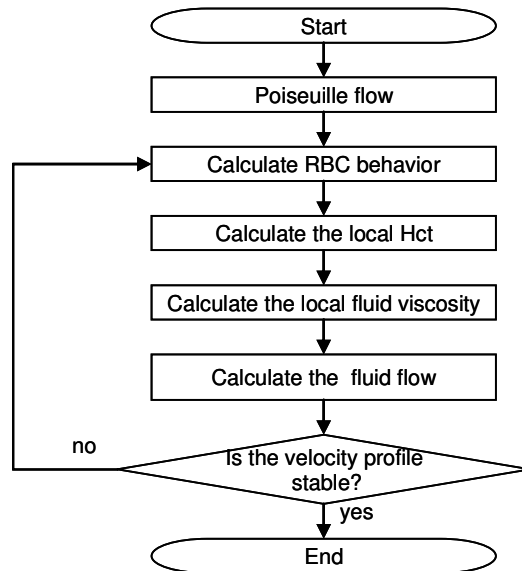
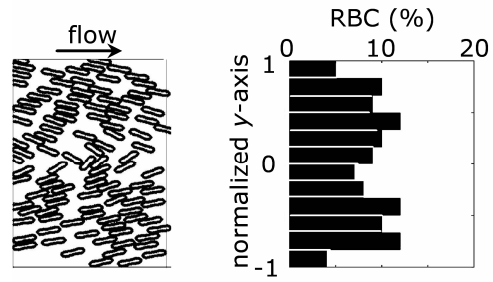
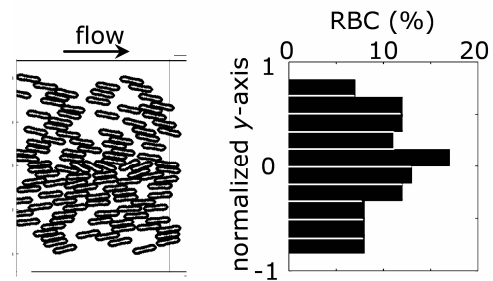


Figure 12. Flowchart of the present simulation



(a) Initial state



(b) Converged state

Figure 13. Comparison of RBC distribution between the initial state (a) and the converged state (b).

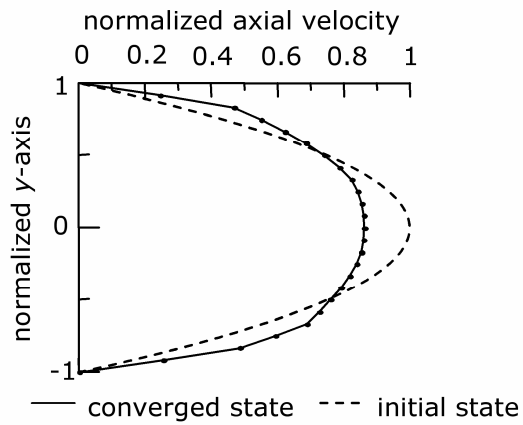


Figure 14. Comparison of the axial velocity profile between the initial and converged states.

### 3.2 Result

The results showed a drastic change in the distribution of RBCs with progress of the simulation. The spatial distributions of RBCs at the initial state and the converged state are shown in Fig. 13. On the right of each figure, the percentage of RBCs in each flow segment at each state is plotted. At the initial state, RBCs were distributed almost uniformly in a radial direction and were found near the wall the initial state. As RBCs were carried downstream by a fluid flow, they inclined and migrated to the center of the flow channel. As a result, RBCs were concentrated around the center and barely found near the wall, forming a plasma layer.

The axial velocity profiles at the initial and converged states are depicted in Fig. 14. At the initial state, the velocity profile was parabolic as given. With progress of the simulation, there was a tendency that velocity at the center of the flow channel decreased while that near the wall increased. At the converged state, the axial flow took a rather flat velocity profile as seen in Fig. 14. The maximal velocity at the converged state decreased by 13.7 % compared to that of the Poiseuille flow.

### 3.3 Discussion

A blood flow property in a small vasculature was analyzed by interactively simulating macro- and micro- scale blood dynamics. The results of the microscale flow simulation showed that RBCs gathered around the center of the flow channel and a plasma layer near the wall at the converged state. On the other hand, the macroscale flow showed a flat velocity profile. These flow features are quite similar to the *in vivo* observations (Oka 1984, Cloutier et al. 1996). It is therefore considered that the simulation results represent the process of how the microscopic flow influences the macroscopic flow.

It is quite obvious that RBC behavior induced a flat velocity profile of the macroscale flow and *vice versa*. With an axial migration of RBCs, the RBC concentration became higher around the center of the channel while that near the wall became less, bringing about an increase in blood viscosity around the center and the decrease near the wall, respectively. As a consequence, the flow velocity around the center of the channel decreased and that near the wall increased, developing into a flat velocity profile.



## 4 Conclusions

Quantitative description of the flow behavior of labeled RBCs in both diluted and concentrated suspensions were studied under a confocal micro-PTV system. The experiments were performed in the middle plane of 75  $\mu\text{m}$  circular PDMS microdevice at low Reynolds numbers ( $Re \sim 0.004$ ) by using Hcts from 3% up to 37%. Our experimental results suggest that the RBC paths are strongly dependent on the Hct and as a result both RBC radial displacement and RBC radial dispersion increase with the hematocrit. Moreover, our results also indicate that RBCs flowing around the plasma layer appear to undergo the largest radial displacements. The confocal micro-PTV system used in the present work is proved to be a powerful technique to measure the motion of labeled RBCs at different Hcts through a circular PDMS microchannel.

A novel computational scheme for the analysis of the mesoscopic blood rheology was proposed. The scheme was applied for the analysis of blood flow in a small vasculature. The simulated flow dynamics were in good agreement with the Casson flow model and *in vivo* observations. These results addressed the potential of the present computational approach to the analysis of the rheology of blood in small vasculatures where non-Newtonian property of blood is significant.

By comparing both results we hope in the near future to clarify a variety of complex phenomena occurring at the microscale level.

## Acknowledgements

This study was supported in part by the following grants: International Doctoral Program in Engineering from the Ministry of Education, Culture, Sports, Science and Technology of Japan (MEXT), “Revolutionary Simulation Software (RSS21)” next-generation IT program of MEXT; Grants-in-Aid for Scientific Research from MEXT and JSPS Scientific Research in Priority Areas (768) “Biomechanics at Micro- and Nanoscale Levels,” Scientific Research (A) No.16200031 “Mechanism of the formation, destruction, and movement of thrombi responsible for ischemia of vital organs”, Grant-in-Aid for Young Scientists (A) 19680024.

## References

- Abramoff M., Magelhaes P., Ram, S. (2004) Image Processing with Image J. *Bio-photonics International* 11: 36-42.
- Caro C., Pedley, T., Schroter R., Seed W. (1978) *The mechanics of the circulation*. Oxford University Press.
- Chien S., Usami S., Skalak R. (1984) Blood flow in small tubes In: *Handbook of Physiology – The cardiovascular system IV*, pp 217-249.
- Cloutier G., Qin Z., Durand L.G., Teh B.G. (1996) Power Doppler ultrasound evaluation of the shear rate and shear stress Dependences of red blood cell aggregation. *IEEE Trans. Biomed. Eng.* 43: 441-450.
- Fahraeus R., Lindqvist T (1931) The viscosity of the blood in narrow capillary tubes. *Am. J. Physiol.* 96: 562-568.
- Goldsmith H. (1971) Red cell motions and wall interactions in tube flow, *Federation Proceedings* 30: 1578-1588.
- Goldsmith H., Marlow J. (1979) Flow behavior of erythrocytes. II. Particles motions in concentrated suspensions of ghost cells, *Journal of Colloid and Interface Science* 71: 383-407.
- Goldsmith H., Turitto V. (1986) Rheological aspects of thrombosis and haemostasis: basic principles and applications. *ICTH-Report-Subcommittee on Rheology of the International Committee on Thrombosis and Haemostasis. Thromb Haemost.* 55: 415–435.
- Ishikawa T., Pedley T., (2007) Diffusion of swimming model micro-organisms in a semi-dilute suspensions. *Journal of Fluid Mechanics* 588: 437-462.
- Lima R., Ishikawa T., Imai, Y., Takeda, M., Wada, S., Yamaguchi, T. (2008a) Microhemodynamic measurements in concentrated suspensions of Red Blood Cells using a confocal micro-PTV system (under revision to *Annals of Biomedical Engineering*).
- Lima R., Ishikawa T., Imai, Y., Takeda, M., Wada, S., Yamaguchi, T. (2008b) Radial dispersion of red blood cells in blood flowing through glass capillaries: role of haematocrit and geometry (under revision to *Journal of Biomechanics*).
- Lima R. (2007) Analysis of the blood flow behavior through microchannels by a confocal micro-PIV/PTV system. PhD Thesis, Tohoku University, Japan.
- Lima R., Wada, S., Takeda, M., Tsubota, K., Yamaguchi, T. (2007a) In vitro confocal micro-PIV measurements of blood flow in a square microchannel: the effect of the haematocrit on instantaneous velocity profiles. *Journal of Biomechanics*, 40: 2752-2757.
- Lima R., Wada, S., Tanaka, S., Takeda, M., Ishikawa, T., Tsubota, K., Imai, Y., Yamaguchi, T. (2008) In vitro blood flow in a rectangular PDMS microchan-

- nel: experimental observations using a confocal micro-PIV system. *Biomedical Microdevices* 10: 153-167.
- Lima R., Wada, S., Tsubota, K., Yamaguchi, T. (2006) Confocal micro-PIV measurements of three dimensional profiles of cell suspension flow in a square microchannel. *Measurement Science and Technology* 17: 797-808.
- Meijering E., Smal I., Danuser G. (2006) Tracking in Molecular Bioimaging, *IEEE Signal Processing Magazine*, 23: 46-53.
- Oka S. (1984) *Biorehology*, Shokabo, Tokyo.
- Park J, Choi C, Kihm K. (2004) Optically sliced micro-PIV using confocal laser scanning microscopy (CLSM). *Experiments in Fluids* 37: 105-119.
- Schmid-Schonbein, H., Wells, R. (1969) Fluid drop-like transition of erythrocytes under shear. *Science* 165: 288-291.
- Shiga T., Maeda N., Suda T., Kon K., Sekiya M., Oka S. (1979) Rheological and kinetic dysfunctions of the cholesterol-loaded, human erythrocytes, *Biorheology*, 16: 363-369.
- Tanaami T, Otsuki S, Tomosada N, Kosugi Y, Shimizu M, Ishida H. (2002) High-speed 1-frame/ms scanning confocal microscope with a microlens and Nipkow disks. *Applied Optics* 41: 4704-4708.
- Wada S., Kobayashi R. (2003) Numerical simulation of various shape changes of a swollen red blood cell by decrease of its volume, *Trans. Jap. Soc. Mech. Eng.* 69A: 14-21 (in Japanese).